

## Superscaling in electroweak excitation of nuclei

M. Martini and G. Co'

*Dipartimento di Fisica, Università di Lecce and Istituto Nazionale di Fisica Nucleare sez. di Lecce, I-73100 Lecce, Italy*

M. Anguiano and A. M. Lallena

*Departamento de Física Atómica, Molecular y Nuclear, Universidad de Granada, E-18071 Granada, Spain*

(Received 28 November 2006; published 9 March 2007)

Superscaling properties of  $^{12}\text{C}$ ,  $^{16}\text{O}$ , and  $^{40}\text{Ca}$  nuclear responses, induced by electron and neutrino scattering, are studied for momentum transfer values between 300 and 700 MeV/c. We have defined two indexes to have quantitative estimates of the scaling quality. We have analyzed experimental responses to get the empirical values of the two indexes. We have then investigated the effects of finite dimensions, collective excitations, meson exchange currents, short-range correlations, and final state interactions. These effects strongly modify the relativistic Fermi gas scaling functions, but they conserve the scaling properties. We used the scaling functions to predict electron and neutrino cross sections and we tested their validity by comparing them with the cross sections obtained with a full calculation. For electron scattering we also made a comparison with data. We have calculated the total charge-exchange neutrino cross sections for neutrino energies up to 300 MeV.

DOI: [10.1103/PhysRevC.75.034604](https://doi.org/10.1103/PhysRevC.75.034604)

PACS number(s): 21.10.Ft, 21.60.-n

### I. INTRODUCTION

The properties of the relativistic Fermi gas (RFG) model of the nucleus [1–3] have inspired the idea of superscaling. In the RFG model, the responses of the system to an external perturbation are related to a universal function of a properly defined scaling variable, which depends on the energy and the momentum transferred to the system. With the adjective universal we want to indicate that the scaling function is independent of the momentum transfer, and also of the number of nucleons. These properties are called, respectively, scaling of the first and second kind. Furthermore, the scaling function can be defined in such a way to result in independence also of the specific type of external one-body operator. This feature is usually called scaling of the zeroth kind [4–6]. One has superscaling when the three kinds of scaling we have described are verified. This happens in the RFG model.

The theoretical hypothesis of superscaling can be empirically tested by extracting response functions from the experimental cross sections and by studying their scaling behaviors. The responses of the nucleus to electroweak probes can be extracted from the lepton-nucleus cross sections by dividing them by the single-nucleon cross sections properly weighted to account for the number of protons and neutrons. In addition, one has to divide the obtained responses by the appropriate electroweak form factors.

Inclusive electron scattering data in the quasi-elastic region have been analyzed in this way [4,7,8]. The main result of these studies is that the longitudinal responses show superscaling behavior. To be more specific, scaling of the second kind, independence of the nucleus, is better fulfilled than the scaling of the first kind, independence of the momentum transfer. The situation for the transverse responses is much more complicated.

The presence of superscaling features in the data is relevant not only by itself but mainly because this property can be used to make predictions. In effect, from a specific set of

longitudinal response data [9], an empirical universal scaling function has been extracted [4] and has been used to obtain neutrino-nucleus cross sections in the quasi-elastic region [5].

We observed that this universal scaling function is quite different from that predicted by the RFG model. This indicates the presence of physical effects not included in the RFG model, but still conserving the scaling properties. We have investigated the superscaling behavior of some of the effects not considered in the RFG model: the finite size of the system, its collective excitations, short-range correlations (SRC), meson exchange currents (MEC), and final state interactions (FSI). The inclusion of these effects produces scaling functions rather similar to the empirical ones.

Before presenting our results, we recall in Sec. II the basic expressions of the superscaling formalism. We show how the scaling functions are related to the electromagnetic and weak response functions, and to the inclusive lepton scattering cross sections.

In Sec. III we discuss the scaling properties of our nuclear models. To quantify the quality of the scaling between the various functions obtained with different calculations, we define two indexes,  $\mathcal{R}$  and  $\mathcal{D}$ . From the data of Ref. [9] we extract empirical reference values of these two indexes that indicate whether scaling has occurred. From the same set of data we also extract an empirical universal scaling function. We analyze the scaling properties of all the effects beyond the RFG model, by comparing the values of the two indexes  $\mathcal{R}$  and  $\mathcal{D}$  of the theoretical scaling functions with the empirical ones. We choose a theoretical scaling function obtained by including all the effects considered as a theoretical universal scaling function.

In Sec. IV we study the prediction power of the superscaling hypothesis. Our universal empirical and theoretical scaling functions are used to calculate electron and neutrino inclusive cross sections. These results are compared with those obtained by calculating the same cross sections with our nuclear model. We discuss results for double differential electron

scattering processes, and we compare our cross sections with experimental data. We also calculate total neutrino cross sections for neutrino energies up to 300 MeV. In Sec. V we summarize our results and present our conclusions.

## II. BASIC SCALING FORMALISM

Scaling variables and functions have been presented in a number of papers [1,4–8,10–13]. The purpose of this section is to recall the expression of the scaling variable used in our study and the relations among scaling functions, responses, and cross sections.

In this work we have considered only processes of inclusive lepton scattering off nuclei. We have described these processes in the plane wave Born approximation and we have neglected the terms related to the rest masses of the leptons. In this presentation we indicate, respectively, with  $\omega$  and  $\mathbf{q}$  the energy and the momentum transferred to the nucleus.

In the RFG model the scaling variables and functions are related to the two free parameters of the model: the Fermi momentum  $k_F$  and the energy shift  $E_{\text{shift}}$ . We define the quantity

$$\Psi_0 = \frac{2m}{k_F} \left[ \sqrt{\left(\frac{\omega - E_{\text{shift}}}{2m}\right) \left(1 + \frac{\omega - E_{\text{shift}}}{2m}\right)} - \frac{q}{2m} \right], \quad (1)$$

where  $q \equiv |\mathbf{q}|$  and  $m = (m_p + m_n)/2$  indicates the average nucleon mass. The scaling variable is then defined as

$$\Psi = \Psi_0 \left( 1 + \Psi_0 \frac{k_F}{2q} \sqrt{\frac{q^2}{m^2} + 1} \right). \quad (2)$$

The RFG model provides a universal scaling function, which can be expressed in terms of the scaling variable  $\Psi$  as [5,6]

$$f^{\text{RFG}}(\Psi) = \frac{3}{4}(1 - \Psi^2)\theta(1 - \Psi^2), \quad (3)$$

where  $\theta(x)$  indicates the step function. The RFG scaling function (3) is normalized to unity.

In the electron scattering case, the inclusive double differential cross section can be written as [14]

$$\frac{d^2\sigma}{d\theta d\omega} = \sigma_M \left\{ \frac{(\omega^2 - q^2)^2}{q^4} R_L(\omega, q) + \left[ \tan^2\left(\frac{\theta}{2}\right) - \frac{\omega^2 - q^2}{2q^2} \right] R_T(\omega, q) \right\}, \quad (4)$$

where  $\theta$  is the scattering angle,  $\sigma_M$  is the Mott cross section, and we have indicated with  $R_L$  and  $R_T$  the longitudinal and transverse responses, respectively, defined as

$$R_L(\omega, q) = 4\pi \sum_{J=0} |\langle J_f || \mathcal{C}_J || J_i \rangle|^2 \quad (5)$$

and

$$R_T(\omega, q) = 4\pi \sum_{J=1} (|\langle J_f || \mathcal{E}_J || J_i \rangle|^2 + |\langle J_f || \mathcal{M}_J || J_i \rangle|^2). \quad (6)$$

In these equations we have indicated with  $|J_i\rangle$  and  $|J_f\rangle$  the initial and final states of the nucleus characterized by their total angular momenta  $J_i$  and  $J_f$ . The double bars indicate that the angular momentum matrix elements are evaluated in their

reduced expressions, as given by the Wigner-Eckart theorem [15]. We have indicated with  $\mathcal{C}_J$ ,  $\mathcal{E}_J$ , and  $\mathcal{M}_J$ , respectively, the Coulomb, electric, and magnetic multipole operators [14,16].

The scaling functions are obtained from the electromagnetic responses as

$$f_L(\Psi) = k_F \frac{q^2 - \omega^2}{q m} \frac{R_L(\omega, q)}{Z(G_E^p)^2 + N(G_E^n)^2}, \quad (7)$$

$$f_T(\Psi) = 2 k_F \frac{q m}{q^2 - \omega^2} \frac{R_T(\omega, q)}{Z(G_M^p)^2 + N(G_M^n)^2}, \quad (8)$$

where  $Z$  and  $N$  indicate, respectively, the number of protons and neutrons of the target nucleus, and we have indicated with  $G_{E,M}^{p,n}$  the electric (E) and magnetic (M) form factors of the proton ( $p$ ) and the neutron ( $n$ ). In our calculations we used the electromagnetic nucleon form factors of Ref. [17]. In Eq. (8) only the magnetic nucleon form factors are present. This implies the hypothesis that in  $R_T$  only the one-body magnetization current is active. In the range of momentum transfer values investigated, from 300 to 700 MeV/c, we found that the contribution of the convection current is of few percents that of the magnetization current.

Since our calculations are done in a nonrelativistic framework, we have modified our responses by using the semi-relativistic corrections proposed in [6,18]:

$$\epsilon \rightarrow \epsilon \left( 1 + \frac{\epsilon}{2m} \right), \quad (9)$$

$$R_L(q, \omega) \rightarrow \frac{q^2}{q^2 - \omega^2} R_L(q, \omega), \quad (10)$$

$$R_T(q, \omega) \rightarrow \frac{q^2 - \omega^2}{q^2} R_T(q, \omega), \quad (11)$$

where  $\epsilon$  indicates the energy of the emitted nucleon.

The discussion here can be extended to the case of the inclusive neutrino scattering processes. For example, for the  $(\nu_e, e^-)$  reaction we express the differential cross section as [19–21]

$$\begin{aligned} \frac{d^2\sigma}{d\Omega d\omega} &= \frac{G^2 \cos^2 \theta_C}{(2\pi)^2} |\mathbf{k}_f| \epsilon_f F(Z', \epsilon_f) \\ &\times \left\{ \left( l_0 l_0^* + \frac{\omega^2}{q^2} l_3 l_3^* - \frac{\omega}{q} l_3 l_0^* \right) R_{CC}^V(\omega, q) \right. \\ &+ l_0 l_0^* R_{CC}^A(\omega, q) + l_3 l_3^* R_{LL}^A(\omega, q) + 2l_3 l_0^* R_{CL}^A(\omega, q) \\ &+ \frac{1}{2} (\vec{l} \cdot \vec{l}^* - l_3 l_3^*) [R_T^V(\omega, q) + R_T^A(\omega, q)] \\ &\left. - \frac{i}{2} (\vec{l} \times \vec{l}^*)_3 R_{TV}^A(\omega, q) \right\}. \quad (12) \end{aligned}$$

In this equation we have indicated with  $G$  the Fermi constant, with  $\theta_C$  the Cabibbo angle, with  $\epsilon_f$  and  $\mathbf{k}_f$  the energy and the momentum of the scattered lepton, and with  $F(Z', \epsilon_f)$  the Fermi function taking into account the distortion of the electron wave function owing to the Coulomb field of the daughter nucleus of charge  $Z'$ . The expressions of the factors  $l_i l_i^*$ , related only to the leptons variables, are given in Refs. [19–21].

The nuclear response functions are expressed in terms of multipole expansion of the operators describing the various terms of the weak interaction. They are the Coulomb  $\mathcal{C}_J$ , longitudinal  $\mathcal{L}_J$ , transverse electric  $\mathcal{E}_J$ , and transverse magnetic  $\mathcal{M}_J$  operators. The responses are defined as

$$R_{\text{CC}}^{\text{V}}(\omega, q) = 4\pi \sum_{J=0} |\langle J_f || \mathcal{C}_J^{\text{V}} || J_i \rangle|^2, \quad (13)$$

$$R_{\text{CC}}^{\text{A}}(\omega, q) = 4\pi \sum_{J=0} |\langle J_f || \mathcal{C}_J^{\text{A}} || J_i \rangle|^2, \quad (14)$$

$$R_{\text{CL}}^{\text{A}}(\omega, q) = 2\pi \sum_{J=0} (\langle J_f || \mathcal{C}_J^{\text{A}} || J_i \rangle^* \langle J_f || \mathcal{L}_J^{\text{A}} || J_i \rangle + \langle J_f || \mathcal{C}_J^{\text{A}} || J_i \rangle \langle J_f || \mathcal{L}_J^{\text{A}} || J_i \rangle^*), \quad (15)$$

$$R_{\text{LL}}^{\text{A}}(\omega, q) = 4\pi \sum_{J=0} |\langle J_f || \mathcal{L}_J^{\text{A}} || J_i \rangle|^2, \quad (16)$$

$$R_{\text{T}}^{\text{V}}(\omega, q) = 4\pi \sum_{J=1} (|\langle J_f || \mathcal{E}_J^{\text{V}} || J_i \rangle|^2 + |\langle J_f || \mathcal{M}_J^{\text{V}} || J_i \rangle|^2), \quad (17)$$

$$R_{\text{T}}^{\text{A}}(\omega, q) = 4\pi \sum_{J=1} (|\langle J_f || \mathcal{E}_J^{\text{A}} || J_i \rangle|^2 + |\langle J_f || \mathcal{M}_J^{\text{A}} || J_i \rangle|^2), \quad (18)$$

and

$$R_{\text{T}}^{\text{VA}}(\omega, q) = 2\pi \sum_{J=1} (\langle J_f || \mathcal{E}_J^{\text{V}} || J_i \rangle^* \langle J_f || \mathcal{M}_J^{\text{A}} || J_i \rangle + \langle J_f || \mathcal{E}_J^{\text{V}} || J_i \rangle \langle J_f || \mathcal{M}_J^{\text{A}} || J_i \rangle^* + \langle J_f || \mathcal{E}_J^{\text{A}} || J_i \rangle^* \langle J_f || \mathcal{M}_J^{\text{V}} || J_i \rangle + \langle J_f || \mathcal{E}_J^{\text{A}} || J_i \rangle \langle J_f || \mathcal{M}_J^{\text{V}} || J_i \rangle^*), \quad (19)$$

where we have separated the vector (V) and the axial-vector (A) contributions.

We found that the terms related to the axial-Coulomb operator  $\mathcal{C}_J^{\text{A}}$  give a very small contribution to the cross section, and, in our study, we neglected them. This means that our scaling analysis has been done for the  $R_{\text{CC}}^{\text{V}}$ ,  $R_{\text{LL}}^{\text{A}}$ ,  $R_{\text{T}}^{\text{V}}$ ,  $R_{\text{T}}^{\text{A}}$ , and  $R_{\text{T}}^{\text{VA}}$  responses only. The corresponding scaling functions have been defined as

$$f_{\text{CC}}^{\text{V}}(\Psi) = k_{\text{F}} \frac{q^2 - \omega^2}{q m} \frac{R_{\text{CC}}^{\text{V}}(\omega, q)}{N(G_{\text{E}}^{(1)})^2}, \quad (20)$$

$$f_{\text{LL}}^{\text{A}}(\Psi) = 4 k_{\text{F}} \frac{q m}{4m^2 + q^2 - \omega^2} \frac{R_{\text{LL}}^{\text{A}}(\omega, q)}{N(G_{\text{A}})^2}, \quad (21)$$

$$f_{\text{T}}^{\text{V}}(\Psi) = 2 k_{\text{F}} \frac{q m}{q^2 - \omega^2} \frac{R_{\text{T}}^{\text{V}}(\omega, q)}{N(G_{\text{M}}^{(1)})^2}, \quad (22)$$

$$f_{\text{T}}^{\text{A}}(\Psi) = 2 k_{\text{F}} \frac{q m}{4m^2 + q^2 - \omega^2} \frac{R_{\text{T}}^{\text{A}}(\omega, q)}{N(G_{\text{A}})^2}, \quad (23)$$

$$f_{\text{T}}^{\text{VA}}(\Psi) = 2 k_{\text{F}} \frac{q m}{\sqrt{q^2 - \omega^2} \sqrt{4m^2 + q^2 - \omega^2}} \frac{R_{\text{T}}^{\text{VA}}(\omega, q)}{N G_{\text{M}}^{(1)} G_{\text{A}}}, \quad (24)$$

where we have indicated with  $G_{\text{E},\text{M}}^{(1)}$  the isovector electric (E) and magnetic (M) nucleon form factors, and with  $G_{\text{A}}$  the axial-vector one. We have used the electromagnetic form factors of

Ref. [17] and the dipole form of the axial vector form factor with an axial mass value of 1030 MeV.

The relativistic effects are taken into account by using semi-relativistic corrections similar to those of Eqs. (9)–(11). In this case the responses are obtained by doing the following changes with respect to the pure nonrelativistic case:

$$R_{\text{CC}}^{\text{V}}(q, \omega) \rightarrow \frac{q^2}{q^2 - \omega^2} R_{\text{CC}}^{\text{V}}(q, \omega), \quad (25)$$

$$R_{\text{LL}}^{\text{A}}(q, \omega) \rightarrow \left(1 + \frac{q^2 - \omega^2}{4m^2}\right) R_{\text{LL}}^{\text{A}}(q, \omega), \quad (26)$$

$$R_{\text{T}}^{\text{V}}(q, \omega) \rightarrow \frac{q^2 - \omega^2}{q^2} R_{\text{T}}^{\text{V}}(q, \omega), \quad (27)$$

$$R_{\text{T}}^{\text{A}}(q, \omega) \rightarrow \left(1 + \frac{q^2 - \omega^2}{4m^2}\right) R_{\text{T}}^{\text{A}}(q, \omega), \quad (28)$$

$$R_{\text{T}}^{\text{VA}}(q, \omega) \rightarrow \sqrt{\frac{q^2 - \omega^2}{q^2}} \sqrt{1 + \frac{q^2 - \omega^2}{4m^2}} R_{\text{T}}^{\text{VA}}(q, \omega). \quad (29)$$

The extension of these expressions to antineutrino charge exchange scattering processes is straightforward. The treatment of charge-conserving processes is slightly different.

### III. SUPERSCALING BEYOND THE RFG MODEL

The basic quantities calculated in our work are the electromagnetic and the weak, nuclear response functions. We obtain the scaling functions by using Eqs. (7) and (8) for the electron scattering case and Eqs. (20)–(24) for the neutrino scattering. The scaling properties of the scaling functions have been studied by a direct numerical comparison. We thought it necessary to define some numerical index able to quantify the quality of the scaling.

Let us consider the problem of comparing a number  $M$  of scaling functions  $\{f_{\alpha}, \alpha = 1, \dots, M\}$ , each of them known for  $K$  values of the scaling variable  $\{\Psi_i, i = 1, \dots, K\}$ . For each value of  $\Psi_i$  we found the maximum and minimum of the various  $f_{\alpha}$  scaling functions:

$$f_i^{\text{max}} = \max_{\alpha=1, \dots, M} [f_{\alpha}(\Psi_i)], \quad (30)$$

$$f_i^{\text{min}} = \min_{\alpha=1, \dots, M} [f_{\alpha}(\Psi_i)]. \quad (31)$$

We define the two indexes

$$\mathcal{D} = \max_{i=1, \dots, K} [f_i^{\text{max}} - f_i^{\text{min}}] \quad (32)$$

and

$$\mathcal{R} = \frac{1}{K f^{\text{max}}} \sum_{i=1, \dots, K} [f_i^{\text{max}} - f_i^{\text{min}}], \quad (33)$$

where  $f^{\text{max}}$  is

$$f^{\text{max}} = \max_{i=1, \dots, K} [f_i^{\text{max}}]. \quad (34)$$

The two indexes give complementary information. The  $\mathcal{D}$  index is related to a local property of the functions: the maximum distance between the various curves. The value of this index could be misleading if the responses have sharp

resonances. For this reason we have also used the  $\mathcal{R}$  index, which is instead sensitive to global properties of the differences between the functions. Since we know that the functions we want to compare are roughly bell shaped, we have inserted the factor  $1/f^{\max}$  to more heavily weight the region of the maxima of the functions than that of the tails.

The perfect scaling is obtained when both  $\mathcal{D}$  and  $\mathcal{R}$  are zero. This is achieved only in the RFG model. In our calculations the perfect scaling is obviously violated, as it is violated by the empirical scaling functions. To have reference values of the two indexes we have determined the values of  $\mathcal{R}$  and  $\mathcal{D}$  for experimental scaling functions extracted from the longitudinal and transverse electromagnetic response data of  $^{12}\text{C}$ ,  $^{40}\text{Ca}$ , and  $^{56}\text{Fe}$  given in Ref. [9]. This is the same set of data used in Ref. [4] to extract a universal scaling function.

The definition of the scaling variable  $\Psi$ , Eqs. (1) and (2), requires one to fix the values of  $k_F$  and  $E_{\text{shift}}$  for each nucleus. We used values of  $k_F$  obtained by doing an average over the nuclear density and used values of  $E_{\text{shift}}$  that, in a Fermi gas calculation, reproduce the peak position of the experimental response functions [22]. We used  $E_{\text{shift}} = 15$  MeV for all the nuclei and  $k_F = 215$  MeV/c for  $^{12}\text{C}$  and  $^{16}\text{O}$  and  $k_F = 245$  MeV/c for  $^{40}\text{Ca}$  and  $^{56}\text{Fe}$ .

The details of the procedures we have used to extract the experimental scaling functions and to calculate the empirical values of  $\mathcal{R}$  and  $\mathcal{D}$  are given in the Appendix. We present in Fig. 1 the experimental longitudinal and transverse scaling function data for  $^{12}\text{C}$ ,  $^{40}\text{Ca}$ , and  $^{56}\text{Fe}$  for each value of the momentum transfer given in Ref. [9]. In Table I we give the values of  $\mathcal{D}$  and  $\mathcal{R}$  obtained by comparing the experimental scaling functions shown in each panel.

We analyze the empirical scaling functions by studying the three different kinds of scaling defined in Sec. I. The presentation of the data of Fig. 1 and Table I gives direct information on the scaling of the second kind. It is immediately observed that, in this case, the  $f_L$  functions scale better than the  $f_T$  ones. The  $f_T$  scaling functions of  $^{12}\text{C}$ , especially for the lower  $q$  values, are remarkably different from those of  $^{40}\text{Ca}$  and  $^{56}\text{Fe}$ . This is confirmed by the values of  $\mathcal{R}$  and  $\mathcal{D}$  given in Table I.

The other two kinds of scaling are not so well fulfilled by the experimental functions. As is evident from the figure, the scaling of the zeroth kind is of poor quality. Longitudinal and transverse scaling functions are remarkably different,

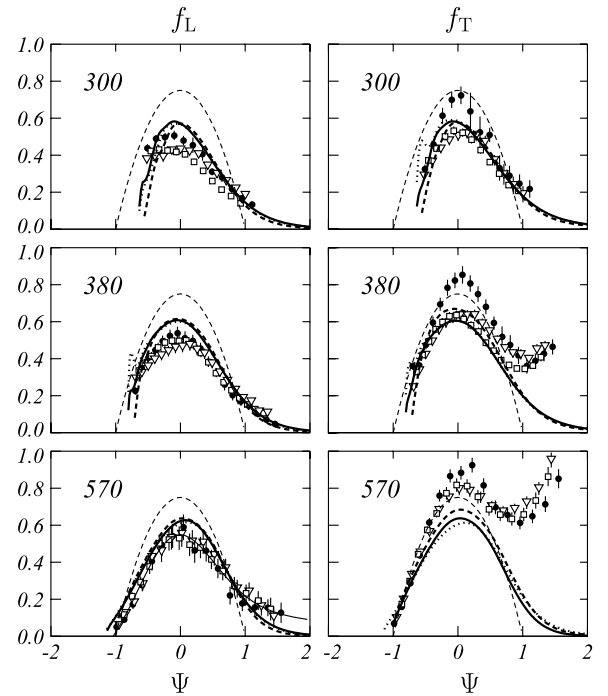


FIG. 1. Empirical longitudinal,  $f_L$ , and transverse,  $f_T$ , scaling functions obtained from the experimental electromagnetic responses of Ref. [9] as explained in the Appendix. The numbers in the panels indicate the values of the momentum transfer in MeV/c. The full circles refer to  $^{12}\text{C}$ , the white squares to  $^{40}\text{Ca}$ , and the white triangles to  $^{56}\text{Fe}$ . The thin black line in the  $f_L$  panel at 570 MeV/c is the empirical scaling function obtained by fitting the data. The thick lines show the results of our calculations when all the effects beyond the RFG model have been considered (see text). The full lines have been calculated for  $^{12}\text{C}$ , the dotted lines for  $^{16}\text{O}$ , and the dashed lines for  $^{40}\text{Ca}$ . The thin dashed lines show the RFG scaling functions.

not only in size, but even in their shapes. The excitation of subnucleonic degrees of freedom, mainly the excitation of the  $\Delta$  resonance, strongly affects  $f_T$ , whereas it is almost irrelevant in  $f_L$ . Also the quality of the scaling of the first kind is rather poor. These observations are in agreement with those of Refs. [4,7,8], where data measured at large  $q$  values have also been used.

From the analysis of the scaling properties of the experimental functions, we have extracted two benchmark values

TABLE I. Values of the  $\mathcal{D}$  and  $\mathcal{R}$  indexes, Eqs. (32) and (33), calculated by comparing the empirical  $f_L$  and  $f_T$  scaling functions shown in Fig. 1 for each value of the momentum transfer  $q$ . The values provide information about the scaling of the second kind. The values of  $\mathcal{D}$  and  $\mathcal{R}$  for  $f_L$  at  $q = 570$  MeV/c, in boldface, are taken as our reference values.

$q$ (MeV/c)	$f_L$		$f_T$	
	$\mathcal{D}$	$\mathcal{R}$	$\mathcal{D}$	$\mathcal{R}$
300	$0.107 \pm 0.002$	$0.152 \pm 0.013$	$0.223 \pm 0.004$	$0.165 \pm 0.017$
380	$0.079 \pm 0.003$	$0.075 \pm 0.009$	$0.235 \pm 0.005$	$0.155 \pm 0.014$
570	<b><math>0.101 \pm 0.009</math></b>	<b><math>0.079 \pm 0.017</math></b>	$0.169 \pm 0.003$	$0.082 \pm 0.007$

of  $\mathcal{R}$  and  $\mathcal{D}$  that we have used to gauge the quality of the scaling of our theoretical functions. The values we have chosen are those related to the  $f_L$  functions at  $q = 570$  MeV/c (see Table I), where the quasi-elastic scattering mechanism works better. In the following, we shall consider that the scaling is violated when  $\mathcal{R} > 0.096$  or  $\mathcal{D} > 0.11$ . These numbers are obtained by adding the uncertainty to the central benchmark values. The nonscaling regions will be indicated by the gray areas in the figures.

From the same set of data we extracted (see the Appendix) an empirical universal scaling function represented by the thin full line in the lowest left panel of Fig. 1. This function, which we called  $f_U^{\text{ex}}$ , is rather similar to the universal empirical function given in Ref. [4].

We start now to consider the scaling of the theoretical functions. The thick lines show the results of our calculations when various effects beyond the RFG are introduced. These scaling functions have been obtained by considering nuclear finite size, collective excitations, short-range correlations, final state interactions, and, in the case of the  $f_T$  functions, meson exchange currents.

The results presented by the thick lines have been obtained for three different nuclei. The full lines represent the  $^{12}\text{C}$  results; the dotted and dashed lines show, respectively, the results obtained for  $^{16}\text{O}$  and  $^{40}\text{Ca}$ . The differences between these curves become larger with decreasing  $q$  values. We obtain  $\mathcal{R} = 0.03$  and  $\mathcal{D} = 0.05$  for  $f_L$  at 570 MeV/c and  $\mathcal{R} = 0.05$  and  $\mathcal{D} = 0.15$  at 300 MeV/c. The scaling of the  $f_T$  functions is not as good. In this case we obtain  $\mathcal{R} = 0.03$  and  $\mathcal{D} = 0.06$  at 570 MeV/c and  $\mathcal{R} = 0.10$  and  $\mathcal{D} = 0.13$  at 300 MeV/c. In any case, these numbers are smaller than our empirical reference values, and we can state that the scaling of the second kind is satisfied.

In contrast, the curves of Fig. 1 show a poor scaling of the first kind. The comparison between the  $f_L$  functions calculated for the three  $q$  values indicated in the figure gives a minimum  $\mathcal{R}$  value of 0.13, found for the  $^{12}\text{C}$  nucleus, and a maximum value of 0.15, found for the  $^{40}\text{Ca}$  nucleus. The minimum and maximum values of the other index,  $\mathcal{D}$ , are 0.18 and 0.30. We found similar (even if a few percent larger) values also for the  $f_T$  functions.

The scaling of the zeroth kind is rather well satisfied. By comparing  $f_L$  and  $f_T$  for each nucleus and each  $q$  value we found 0.04 as a maximum value of  $\mathcal{R}$ . We found 0.11 for  $\mathcal{D}$ , slightly large even if below our empirical limiting value. This relatively large value of  $\mathcal{D}$  is due to the presence of sharp resonances in the longitudinal and transverse responses at  $q = 300$  MeV/c, which appear at different excitation energies. We have chosen the longitudinal scaling function obtained for  $^{16}\text{O}$  at  $q = 570$  MeV/c as the theoretical universal scaling function that we called  $f_U^{\text{th}}$ .

In Fig. 1 the thin dashed lines show the RFG scaling functions. It is evident that the inclusion of the effects beyond the RFG we have considered produce relevant modifications of the RFG scaling functions. These modifications remarkably improve the agreement with the experimental scaling functions. However, the effects we have considered do not heavily modify the scaling properties of the  $f_L$  and  $f_T$  functions. In the remaining part of the section, we first discuss the consequences

of each effect beyond RFG, and then we analyze the scaling properties for neutrino scattering processes.

### A. Finite-size effects

The starting point of our calculations is the continuum shell model. In this model, the scattering processes are described by using some of the assumptions on the nuclear structure that are also used in the Fermi gas model. We refer to the fact that both nuclear models consider the nucleons free to move in a mean-field potential. The continuum shell model takes into account the finite dimensions of the system, the finite number of nucleons, and the fact that protons and neutrons feel different mean-field potentials. In our calculations, the mean field is produced by a Woods-Saxon well. The parameters of this potential are taken from Refs. [23] (for  $^{12}\text{C}$ ) and [24] (for  $^{16}\text{O}$  and  $^{40}\text{Ca}$ ) and have been fixed to reproduce the single particle energies around the Fermi surface and the rms radii of the charge distributions of each nucleus we have considered.

The scaling properties of this model have been verified in Ref. [6] for  $q$  values larger than 700 MeV/c. We are interested in the region of lower  $q$  values, and we have calculated longitudinal and transverse responses for momentum transfer values down to 300 MeV/c. Our results are summarized in Fig. 2. In panels (a) and (b) of the figure the thick lines show the  $f_L$  scaling functions obtained, respectively, for  $q = 300$  MeV/c and  $q = 700$  MeV/c, the extreme values used in our calculations. The full, dotted and dashed lines indicate the  $^{12}\text{C}$ ,  $^{16}\text{O}$ , and  $^{40}\text{Ca}$  results, respectively, whereas the thin dashed lines show the RFG model ones. As expected, for  $q = 300$  MeV/c, shell model and RFG produce rather different scaling functions. The shell-model results present sharp resonances, and the figure indicates that the scaling of the second kind is poorly satisfied. The situation changes with increasing momentum transfer. For  $q = 700$  MeV/c the  $f_L$  values show excellent scaling of the second kind and the agreement with the RFG results has largely improved. Our scaling functions do not have their maxima exactly at  $\Psi = 0$  and present a small left-right asymmetry.

More concise information about the scaling properties of these results is given in the other two panels of Fig. 2. In panel (c) the values of  $\mathcal{R}$  and  $\mathcal{D}$  are calculated by comparing the  $f_L$  and  $f_T$  scaling functions of the same nucleus, for a fixed  $q$  value. The results shown in panel (c) give information on how the scaling of the zeroth kind is verified at each  $q$  value. In this panel, the black circles show the  $^{12}\text{C}$  results, the black triangles the  $^{16}\text{O}$  results, and the white squares the  $^{40}\text{Ca}$  results. The general trend is an increase of the index values at low  $q$ . In any case, all the values of the indexes shown in this panel are well below the empirical ones, indicating the good quality of the scaling.

The results shown in panel (d) have been obtained by using the following procedure. For each nucleus, we have calculated the scaling functions from  $q = 300$  MeV/c to  $q = 700$  MeV/c, in steps of 50 MeV/c. The curves show the values of the indexes  $\mathcal{R}$  and  $\mathcal{D}$  obtained by considering in Eqs. (32) and (33) all the  $f_L$  values calculated from the  $q$  value indicated in the figure, up to  $q = 700$  MeV/c. Evidently, these curves are zero at

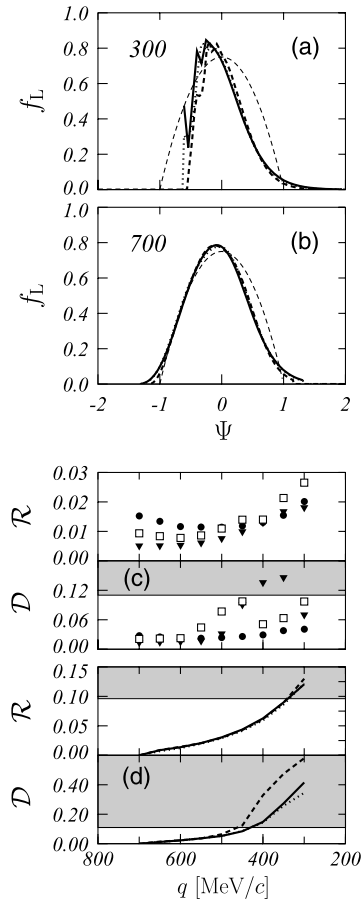


FIG. 2. Continuum shell-model results. In panels (a) and (b), the thick lines represent the  $f_L$  scaling functions calculated for the various nuclei: full lines,  $^{12}\text{C}$ ; dotted lines,  $^{16}\text{O}$ ; dashed lines,  $^{40}\text{Ca}$ . The thin dashed lines represent the RFG scaling function. The numbers inside the panels indicate the values of the momentum transfer in MeV/c units. In panel (c) we show for each nucleus the values of the indexes  $\mathcal{R}$  and  $\mathcal{D}$  obtained at a fixed  $q$  value by comparing the  $f_L$  and  $f_T$  functions. The black circles indicate the  $^{12}\text{C}$  results, the black triangles those of  $^{16}\text{O}$ , and the white squares those of  $^{40}\text{Ca}$ . In panel (d) we show the value of the two indexes obtained by considering the  $f_L$  functions calculated for all the momentum transfer values ranging from the indicated  $q$  value up to 700 MeV/c. Details of the procedure are given in the text. As in panels (a) and (b), the full lines refer to  $^{12}\text{C}$ , the dotted ones to  $^{16}\text{O}$ , and the dashed ones to  $^{40}\text{Ca}$ . The gray areas, drawn above the empirical values of  $\mathcal{R}$  and  $\mathcal{D}$ , indicate the non-scaling region.

$q = 700$  MeV/c and increase continuously with decreasing  $q$  values. Panel (d) shows the evolution of the scaling of the first kind with decreasing  $q$  values. In panel (d) the full lines show the  $^{12}\text{C}$  results, and the dotted and dashed lines show those of  $^{16}\text{O}$  and of  $^{40}\text{Ca}$ , respectively. If the scaling of the first kind is verified, the values of  $\mathcal{R}$  and  $\mathcal{D}$  in this panel are constant. We observe that all the curves lie below the empirical benchmark limits until the scaling function obtained for  $q = 400$  MeV/c is included. This could be considered the lower  $q$  limit where the scaling of the first kind is broken by nuclear finite size effects.

## B. Collective excitations

By definition, mean-field models, such as the RFG model or the shell model, do not describe collective excitations of the nucleus. We have considered the contribution of these excitations within a continuum random phase approximation (RPA) framework. Details of our RPA calculations are given in Ref. [23]. In the present work, we used two effective nucleon-nucleon interactions. They are a zero-range interaction of Landau-Migdal type, called LM1 in [23], and the finite-range polarization potential of Ref. [25], properly renormalized as indicated in [23], and labeled PP.

Before discussing the results of the RPA calculations, we want to point out a technical detail of our calculation. The semi-relativistic prescription (9) cannot be coherently implemented in the continuum RPA equations. We have calculated the continuum RPA responses without the semi-relativistic correction. The scaling functions have been obtained from these responses by using the nonrelativistic definition of the scaling variable [2]:

$$\Psi = \frac{1}{k_F} \left[ \frac{m(\omega - E_{\text{shift}})}{q} - \frac{q}{2} \right]. \quad (35)$$

With this scaling variable, the superscaling function of the nonrelativistic Fermi gas model assumes again the expression of Eq. (3) (see Ref. [2]).

The comparison between the Fermi gas scaling function and  $f_L$  and  $f_T$  calculated with the RPA is presented in Fig. 3. In this figure, we show the  $^{12}\text{C}$  scaling functions obtained for the two extreme values of  $q$  considered in our calculations. The thick full lines show the mean-field results, the dotted lines the results obtained with the LM1 interaction, and the dashed lines those obtained with the PP interaction.

The scaling functions at  $q = 300$  MeV/c are strongly affected by the RPA. This was expected, since for this value

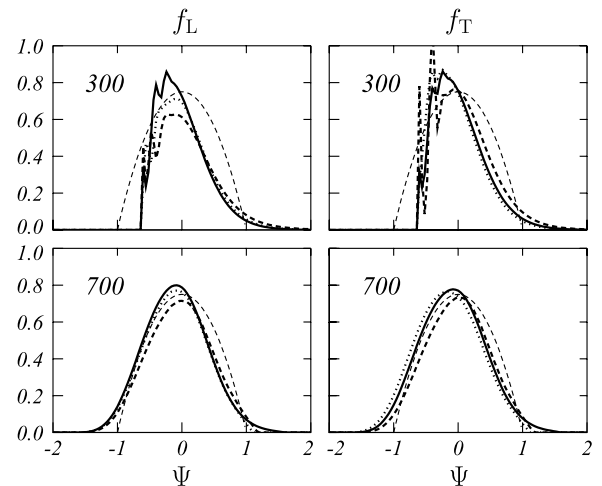


FIG. 3. Scaling functions calculated for the  $^{12}\text{C}$  nucleus. The thin dashed lines show the Fermi gas results. The full lines show the mean-field results. The other lines have been obtained by using the continuum RPA. The thick dotted lines show the results obtained with the PP interaction, whereas the thick dashed lines have been obtained by using the LM1 interaction. The numbers in the panels indicate the values of the momentum transfer in MeV/c units.

of the momentum transfer, the maxima of the electromagnetic responses are very close to the giant resonance region. The situation is rather different for the case of 700 MeV/c, where the mean-field and RPA scaling functions are very similar. Here, the RPA effects are larger for zero-range than for finite-range interaction. The explanation of this fact becomes evident if one considers the ring approximation of the RPA propagator for an infinite system [26]:

$$\Pi^{\text{RPA}}(q, \omega) = \frac{\Pi^0(q, \omega)}{1 - V(q)\Pi^0(q, \omega)}, \quad (36)$$

where  $\Pi^0$  indicates the free Fermi gas polarization propagator and  $V(q)$  is a purely scalar interaction. Finite-range interactions vanish at large  $q$  values; therefore the RPA propagator becomes equal to that of the Fermi gas. This does not happen if contact interactions are used, since these interactions are constant in momentum space. We found that, for  $q$  values larger than 500 MeV/c, the RPA effects are negligible if calculated with a finite-range interaction.

The scaling properties of continuum RPA  $f_L$  and  $f_T$  calculated for  $^{12}\text{C}$  are summarized in Fig. 4. The lines in this figure have been calculated with the same procedure used in Fig. 2(d). The full lines represent the mean-field results, the dotted lines show the results obtained with the finite-range interaction, and the dashes lines have been obtained with the zero-range interaction. The figure shows that scaling of

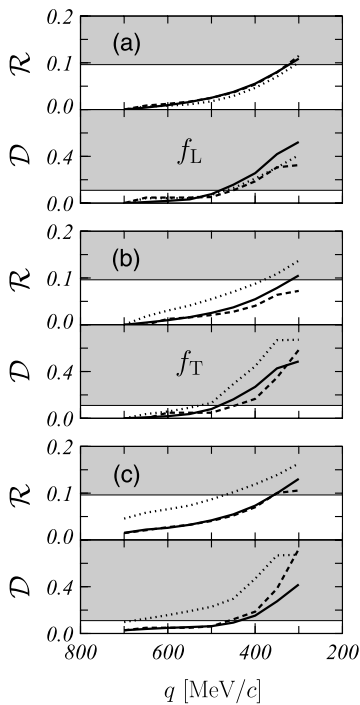


FIG. 4. The  $\mathcal{R}$  and  $\mathcal{D}$  indexes calculated as in panel (d) of Fig. 2. In panels (a) and (b) the  $f_L$  and  $f_T$  scaling functions calculated for the  $^{12}\text{C}$  nucleus are separately shown. In panel (c) the indexes have been calculated by comparing the  $f_L$  and  $f_T$  scaling functions. The full lines represent the mean-field results, whereas the dotted and dashed lines have been obtained by doing continuum RPA calculations, respectively, with the polarization potential and with the Landau-Migdal interaction.

the first kind is well preserved by RPA calculations up to  $q = 400$  MeV/c. In (c) the  $f_L$  and  $f_T$  scaling functions have been put together in the calculation of the two indexes. We observe a worsening of the scaling, especially for the polarization potential results. This indicates that scaling of the zeroth kind is slightly ruined by the RPA. This is understandable, since the effective nucleon-nucleon interaction acts in a different manner on the longitudinal and on the transverse nuclear responses. Finally, scaling of the second kind is well preserved also in the RPA calculations.

### C. Meson exchange currents

We have seen that collective excitations are different in longitudinal and transverse responses and this breaks the scaling of the zeroth kind. However, our RPA results show that these effects are too small to explain the large differences between experimental  $f_L$  and  $f_T$  shown in Fig. 1. Another possible source of the breaking of the zeroth-kind scaling is provided by the MEC. Their role in the longitudinal responses is negligible [27], whereas they can be relevant in the transverse responses.

We have calculated the transverse response functions by adding to the one-body convection and magnetization currents the MEC arising from the exchange of a single pion. In Fig. 5 we show the Feynman diagrams of the MEC we have considered. They are (a) the seagull, or contact, term, where the virtual photon interacts at the pion-nucleon vertex, and (b) the pionic, or pion in flight, term, where the virtual photon interacts with the exchanged pion. In addition we also consider the  $\Delta$  current terms, where the photon excites, or de-excites, a virtual  $\Delta$  resonance, which interacts with another nucleon by exchanging a pion. These  $\Delta$  current terms are represented by diagrams (c) and (d) of Fig. 5. A detailed description of our MEC model is given in Refs. [28–30].

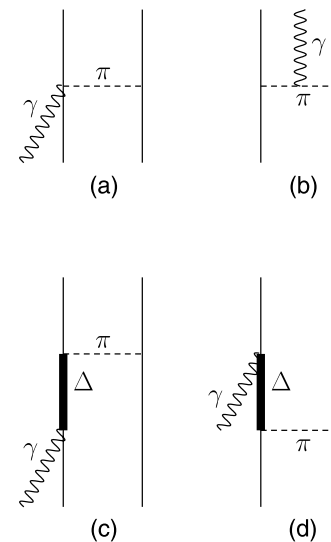


FIG. 5. Feynman diagrams of the MEC terms considered in our calculations. Diagrams (a) and (b) represent, respectively, the seagull and pionic currents; the other two diagrams show the  $\Delta$  currents.

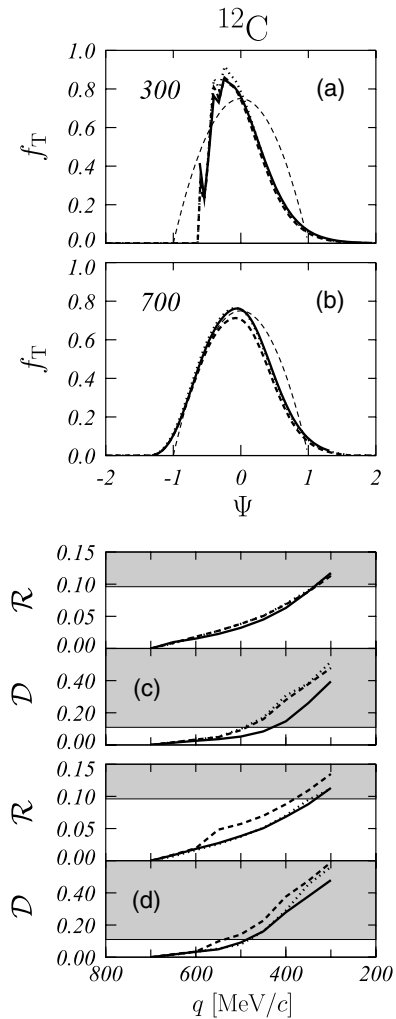


FIG. 6. Transverse scaling functions for the  $^{12}\text{C}$  nucleus. In panels (a) and (b), the thin dashed lines show the RFG model. The other, thick, lines have been obtained by using the continuum shell model. The full lines show the results obtained by using one-body currents only. The dotted lines have been obtained by inserting the pionic and seagull terms of the MEC, and the dashed lines show the results obtained by including also the  $\Delta$  currents. The numbers inside the panels indicate the values of the momentum transfer in MeV/c. The curves in panels (c) and (d) are calculated as in panel (d) of Fig. 2. The curves in (c) compare the results obtained in  $^{12}\text{C}$  by using one-body currents only (full line) with those obtained by adding seagull and pionic MEC (dotted line) and by adding also the  $\Delta$  currents (dashed lines). In panel (d) we compare the results obtained with all the MEC for the three nuclei considered. The full line shows the  $^{12}\text{C}$  result, the dotted line the  $^{16}\text{O}$  result, and the dashed line the  $^{40}\text{Ca}$  result.

We show in panels (a) and (b) of Fig. 6 the  $f_T$  scaling functions of the  $^{12}\text{C}$  nucleus calculated for the extreme  $q$  values we have considered. The full lines have been obtained by using one-body currents only, the dotted lines by including seagull and pionic currents, and the dashed lines by adding the  $\Delta$  currents. As usual, the thin dashed lines show the RFG scaling function.

The effects of the MEC on the scaling functions are analogous to those found on the responses in Ref. [31]. The seagull and pionic terms produce effects of opposite sign; therefore, the changes with respect to the one-body responses are rather small, and they almost vanish for the largest values of  $q$  we have considered. The inclusion of the  $\Delta$  currents slightly decreases the values of the scaling functions. The presence of these currents becomes more relevant with increasing  $q$  value.

Panel (c) of Fig. 6 shows the values of  $\mathcal{R}$  and  $\mathcal{D}$ , calculated for  $f_T$  as in panel (d) of Fig. 2, for  $^{12}\text{C}$ . The meaning of the different curves is the same as in the two upper panels of the figure. In panel (d) we show the behavior of the two indexes calculated for the  $f_T$  scaling functions when all the MEC are included. The full lines show the  $^{12}\text{C}$  results, the dotted lines the  $^{16}\text{O}$  results, and the dashed lines the  $^{40}\text{Ca}$  results.

Our MEC conserve rather well the scaling properties of  $f_T$ . The shapes of the  $f_T$ , shown in the upper panels of Fig. 6, are rather different from those of the empirical  $f_T$ , given in Fig. 1. Our MEC model considers only virtual excitations of the  $\Delta$  resonance, which become more important at large  $q$  values. All these observations indicate that the origin of the high-energy tail of the experimental transverse scaling functions is the real excitation of the  $\Delta$  resonance, with the consequent production of pions.

#### D. Short-range correlations and final state interactions

As already mentioned, we have also investigated the influence of SRC. Our results are summarized in Fig. 7, where, in panel (a), we show, as an example, the  $f_L$  scaling function of  $^{12}\text{C}$  calculated for  $q = 700$  MeV/c with (dashed lines) and without (full curves) SRC. The same curves are plotted in both linear and logarithmic scales, to show the eventual effects in the tails of the distributions.

The calculation of the responses with the SRC is done as described in [32], by considering all the cluster terms containing a single correlation line. This implies the evaluation of two- and three-point cluster terms, which produce contributions of different sign. The calculations have been done with the scalar correlation function labeled EU (Euler) in [24]. The effects of the correlations on the momentum distribution of  $^{12}\text{C}$  are shown in panel (b) of Fig. 7. Also this momentum distribution has been calculated in a first-order approximation [33]. This example shows that the scaling functions, in the kinematics of our interest, are insensitive to the high-momentum tail of the momentum distribution and, in general, to the SRC.

None of the results we have so far presented have included FSI, which produce the largest modifications of the mean-field responses [34]. We treat the FSI by using the model developed in Refs. [35,36]. The mean-field responses are folded with Lorentz functions whose parameters have been extracted from optical potential volume integrals, and from the empirical spreading widths of single-particle states. This approach has been successfully used to describe quasi-elastic electromagnetic responses [31,35], and, more recently, it has been applied to calculate neutrino scattering cross sections [23,37,38].

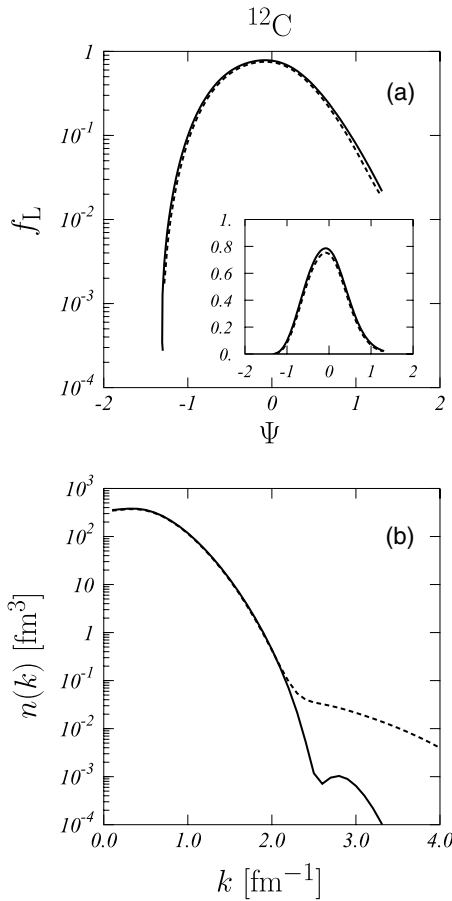


FIG. 7. (a) The longitudinal scaling function of  $^{12}\text{C}$  calculated for  $q = 700$  MeV/c. The full lines show the mean-field result; the dashed lines have been obtained by including the SRC. In the insert, the same results are shown on a linear scale. (b) The momentum distribution of  $^{12}\text{C}$  calculated with the mean-field model (full line) and with the SRC (dashed line).

In the two upper panels of Fig. 8 we show the shell-model  $f_L$  scaling functions corrected for the presence of the FSI. Again, we show here the results obtained for the two extreme values of  $q$  considered in our calculations. The thin dashed lines show the RFG results. It is evident that the FSI are responsible for the largest modifications of the mean-field results. The values of the maxima of the scaling functions in Fig. 2 are around 0.8. After the inclusion of the FSI, these maxima are of the order of 0.6. The FSI lower the values of the maxima of the responses and, since the total area is conserved, increase their widths.

The presence of the FSI slightly worsens the almost perfect scaling of the zeroth kind shown in Fig. 2. The FSI act differently on the two responses. The longitudinal responses are insensitive to the spin and spin-isospin terms of the nuclear interaction. This fact is considered in our FSI model. Even though in panel (c) of Fig. 8 the values of  $\mathcal{R}$ , calculated for each  $q$  value, are slightly larger than the analogous ones of Fig. 2, they are below the empirical value. The case of the  $\mathcal{D}$  index is curious, since it shows almost constant values. This is because  $\mathcal{D}$  indicates the maximum difference between the various curves considered. The FSI produce a smoothing of

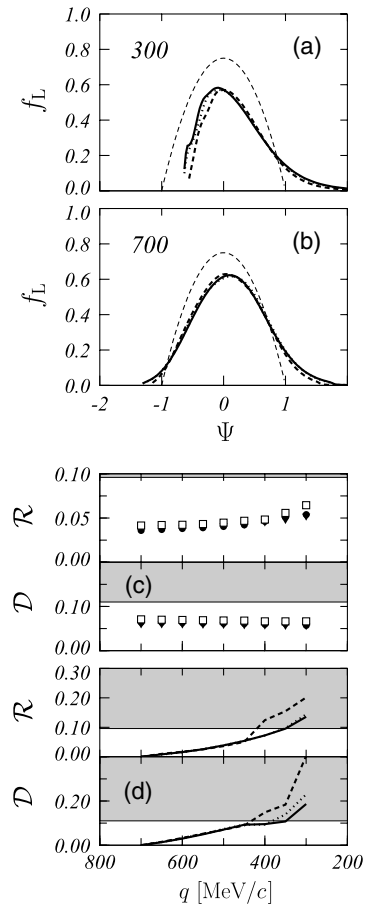


FIG. 8. The same as Fig. 2 but showing the results of the mean-field model with FSI.

these curves and cancel the sharp resonant peaks that appear at low  $q$  values.

The curves in panel (d) are obtained in the same way as those of the analogous panel in Fig. 2. The values shown in Fig. 8 are clearly larger than those of panel (d) of Fig. 2. For the  $\mathcal{R}$  index, the non-scaling gray area is reached when the  $q$  value is about 500 MeV/c. In conclusion, the FSI produce large modifications of the mean-field responses, but they do not strongly violate the scaling.

### E. Neutrino scaling functions

Up to now, we have discussed the scaling properties of the electromagnetic scaling functions. We present in Fig. 9 the scaling functions defined in Eqs. (20)–(24), for the  $(\nu_e, e^-)$  charge exchange reaction. The thick lines of the two upper panels show the five scaling functions calculated, in a continuum shell model, for the  $^{16}\text{O}$  nucleus, and for the two extreme values of  $q$  considered in our work. The five curves are rather well overlapped at  $q = 300$  MeV/c, and they almost exactly overlapped at  $q = 700$  MeV/c. The agreement with the RFG result, indicated as usual by the dashed thin lines, is rather good at  $q = 700$  MeV/c.

In panel (c) we show the  $\mathcal{R}$  and  $\mathcal{D}$  indexes calculated by comparing the five scaling functions at each  $q$  value indicated

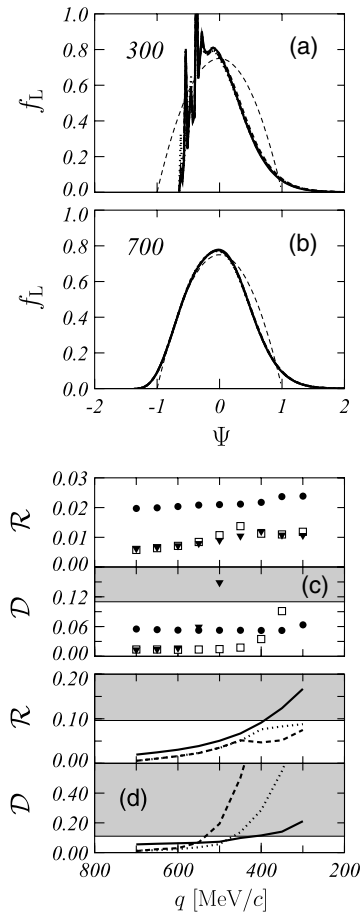


FIG. 9. The same as Fig. 2 for the neutrino scaling functions. In both panels (a) and (b) the five scaling functions defined in Eqs. (20)–(24) and calculated for the  $^{16}\text{O}$  nucleus are shown by the thick lines. These lines are almost exactly overlapped. Again the dashed thin lines show the RFG scaling functions. In panel (c) the indexes are calculated by comparing the five scaling functions calculated at each  $q$  value indicated on the  $x$  axis. The black dots show the  $^{12}\text{C}$  results, the triangles the  $^{16}\text{O}$  results, and the white squares the  $^{40}\text{Ca}$  results. The values for the two indexes shown in panel (d) have been calculated as in the analogous panel of Fig. 2. The full line refers to  $^{12}\text{C}$ , the dotted one to  $^{16}\text{O}$ , and the dashed one to  $^{40}\text{Ca}$ .

in the  $x$  axis. The black circles show the  $^{12}\text{C}$  results, the black triangles those of  $^{16}\text{O}$ , and the white squares the  $^{40}\text{Ca}$  results. These values are of the same order of magnitude as those of (c) panel of Fig. 2. This confirms the observation that scaling of the zeroth kind is well satisfied in continuum shell-model calculations.

In panel (d) the values of the two indexes are evaluated by doing a comparison of the scaling functions calculated at  $q = 700$  MeV/c with those obtained for lower  $q$  values. This indicates the validity of scaling of the first kind. The index  $\mathcal{R}$  shows that there is a reasonable scaling down to  $q = 400$  MeV/c. This value is analogous to that found for the electromagnetic functions. The index  $\mathcal{D}$  shows much rapid variations and, already at  $q = 500$  MeV/c, its value is over the

empirical limiting value. This is due to the presence of sharp resonances at low  $q$  values in some of the responses.

We studied the effects beyond the RFG for charge exchange neutrino responses, by following the same steps used for the electromagnetic responses. To be precise, we did not calculate responses with SRC or with the MEC, since from the results obtained for the electromagnetic responses, we do not expect large changes of the mean-field results due to these effects. We found effects of RPA and FSI analogous to those of the electromagnetic case.

#### IV. SUPERSCALING PREDICTIONS

In the previous section we have studied how the effects beyond the RFG model modify the scaling function. We found that the main effects are produced by the FSI. Despite the large modifications of the RFG scaling functions, the scaling properties are not heavily destroyed. For momentum transfer values above 500 MeV/c, our scaling functions present values of the scaling indexes smaller than the empirical benchmarks. After having established the range of validity of the superscaling hypothesis, we investigate, in this section, its prediction power. The strategy of our investigation consists in comparing responses and cross sections, calculated by using RPA, FSI, and eventually MEC and SRC, with those obtained by using our universal scaling functions, both  $f_U^{\text{ex}}$  and  $f_U^{\text{th}}$ . All the RPA calculations presented in this section have been made by using the PP interaction.

The first test case of our study is done on the double differential electron scattering cross section. We show in Fig. 10 the inclusive electron scattering cross sections calculated with our model including the MEC and the FSI effects (full lines), those obtained with  $f_U^{\text{th}}$  (dashed lines), and the cross sections obtained with  $f_U^{\text{ex}}$  (dotted lines). These results are compared with the data of Refs. [39–41].

The first remark about Fig. 10 regards the excellent agreement between the results of the full calculations with those obtained by using  $f_U^{\text{th}}$ . This clearly indicates the validity of the scaling approach in this kinematic region. This result was expected from the studies of the previous section, since in all the cases shown in Fig. 10, the value of the momentum transfer is larger than 500 MeV/c. The differences with the cross sections obtained by using the empirical scaling functions reflect the differences among the various scaling functions shown in Fig. 1.

A second remark regarding Fig. 10 is that our results underestimate the data. Probably this is because the excitation of the  $\Delta$  resonance is not considered in our calculations. The behavior of the data of the figure in the higher energy part shows the presence of the  $\Delta$  resonance. The low-energy tail of the excitation of this resonance also affect the quasi-elastic peak.

The situation for the double differential cross sections is well controlled, since all the kinematic variables, beam energy, scattering angle, and energy of the detected lepton are precisely defined and, consequently, energy and momentum are also transferred to the nucleus. The situation changes for the total cross sections, which are of major interest for the neutrino physics. The total cross sections are only functions of the

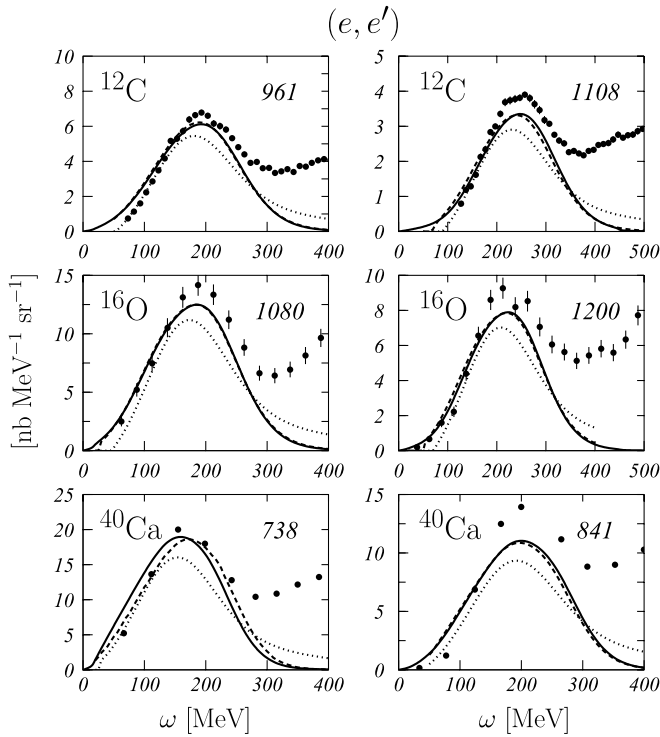


FIG. 10. Inclusive electron scattering cross sections. Here, the numbers in the panels indicate, in MeV, the energy of the incoming electron. The  $^{12}\text{C}$  data [39] have been measured at a scattering angle of  $\theta = 37.5^\circ$ , the  $^{16}\text{O}$  data [40] at  $\theta = 32.0^\circ$ , and the  $^{40}\text{Ca}$  data [41] at  $\theta = 45.5^\circ$ . The full lines show the results of our complete calculations. The cross sections obtained by using  $f_U^{\text{th}}$  are shown by the dashed lines, and those obtained with  $f_U^{\text{ex}}$  are given by the dotted lines.

energy of the incoming lepton; therefore they consider all the scattering angles and the possible values of the energy and momentum transferred to the nucleus, with only the limitation of the global energy and momentum conservations. This means that, in the total cross sections, kinematic situations where the scaling is valid and also where it is not valid are both present.

To clarify this point with quantitative examples, we show in Fig. 11 various differential charge-exchange cross sections obtained for 300 MeV neutrinos on an  $^{16}\text{O}$  target. In panel (a) we show the double differential cross sections calculated for a scattering angle of  $30^\circ$ , as a function of the nuclear excitation energy. The full line shows the result of our complete calculation, done with continuum RPA and FSI. We have shown in the previous section that the effects of MEC and SRC are negligible in this kinematic regime. The dashed line shows the result obtained with  $f_U^{\text{th}}$  and the dotted line those with  $f_U^{\text{ex}}$ . The values of the momentum transfer vary from about 150 to 200 MeV/c. Evidently, this is not the quasi-elastic regime where the scaling is supposed to hold, and this evidently produces the large differences among the various cross sections.

The cross sections integrated on the scattering angle are shown as a function of the nuclear excitation energy in panel (b) of the figure; the cross sections integrated on the excitation energy as a function of the scattering angle are shown in panel (c).

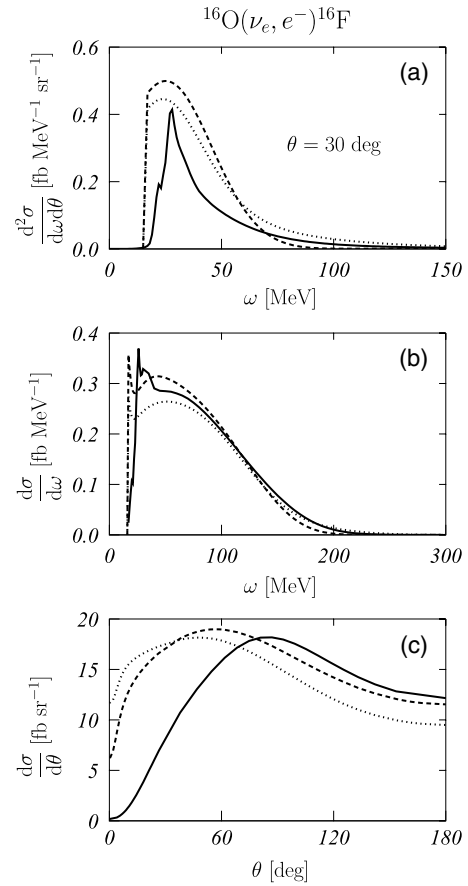


FIG. 11. Neutrino charge exchange cross sections on  $^{16}\text{O}$ . All the results shown in the various panels have been obtained for a neutrino energy of 300 MeV. In all the panels the full lines show the result of our complete calculation; the other lines show the results obtained by using the scaling functions. Specifically, the dashed and the dotted lines have been obtained, respectively, with  $f_U^{\text{th}}$  and  $f_U^{\text{ex}}$ . In panel (a) the double differential cross sections calculated for the scattering angle of  $30^\circ$  as a function of the nuclear excitation energy are shown. In panel (b) we show the cross sections integrated on the scattering angle, always as a function of the nuclear excitation energy. In panel (c) we show the cross sections integrated on the nuclear excitation energy, as a function of the scattering angle.

The three panels of the figure illustrate in different manner the same physics issue. The calculation with the scaling functions fails to reproduce the results of the full calculation in the region of low energy and low momentum transfer, where surface and collective effects are important. This is shown in panel (b) by the bad agreement among the three curves in the lower energy region, and in panel (c) at low values of the scattering angle, where the  $q$  values are minimal.

Total charge-exchange neutrino cross sections are shown in Fig. 12 in both linear and logarithmic scale, as a function of the energy of the incident neutrino  $\epsilon_i$ . As in the previous figure, the full lines show the result of the full calculation, whereas the dashed and dotted lines have been obtained, respectively, with  $f_U^{\text{th}}$  and  $f_U^{\text{ex}}$ . The scaling predictions for neutrino energies up to 200 MeV are unreliable. These total cross sections are obviously dominated by the giant resonances, and more

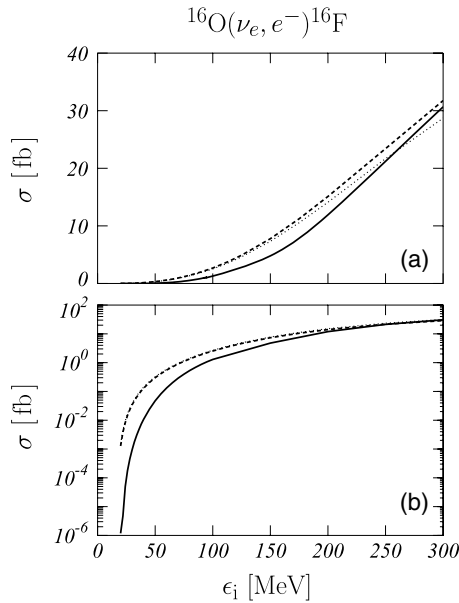


FIG. 12. Total neutrino cross sections. Both panels show the same results in linear (a) and logarithmic (b) scales. The full lines show the result of the complete calculations. The dashed lines have been obtained by using  $f_U^{\text{th}}$ , and the dotted lines by using  $f_U^{\text{ex}}$ .

generally by collective nuclear excitation. We have seen that these effects strongly violate the scaling. At  $\epsilon_i = 200$  MeV the cross section obtained with  $f_U^{\text{th}}$  is about 20% larger than those obtained with the full calculation. This difference becomes smaller with increasing energy and is about 7% at  $\epsilon_i = 300$  MeV. This is an indication that the relative weight of the nonscaling kinematic regions become smaller with increasing neutrino energy.

## V. SUMMARY AND CONCLUSIONS

We have investigated the scaling properties of the electron and neutrino cross sections in a kinematic region involving momentum transfer values smaller than 700 MeV/c. Since our working methodology implies the numerical comparison of different scaling functions, we defined two indexes, Eqs. (32) and (33), to provide a quantitative indication of the scaling quality.

We have first analyzed the scaling properties of the experimental electromagnetic responses given in Ref. [9] for the  $^{12}\text{C}$ ,  $^{40}\text{Ca}$ , and  $^{56}\text{Fe}$  nuclei. We found the better scaling situation for the longitudinal responses at 570 MeV/c. By considering these data we obtained empirical values of the two indexes that we consider the upper acceptable limit to have scaling. From a fit to the same set of data we have also obtained an empirical scaling function,  $f_U^{\text{ex}}$ .

Our study of the role played by effects beyond the RFG model on the scaling properties of the electroweak responses consisted in comparing the values of the indexes obtained in our calculations with the empirical values. We found that finite-size effects conserve scaling of the first kind, the most likely violated, down to 400 MeV/c. We have estimated the effects of the collective excitations by doing continuum

RPA calculations with two different residual interactions. RPA effects become smaller as the value of the momentum transfer becomes larger. At momentum transfer values above 600 MeV/c RPA effects are negligible if calculated with a finite-range interaction, whereas zero-range interactions produce larger effects. Collective excitations break scaling properties. We found that scaling of the first kind is satisfied down to about 500 MeV/c.

The presence of the MEC violates the scaling of the transverse responses. From the quantitative point of view, MEC effects, at relatively low  $q$  values, are extremely small. In our model, MEC start to be relevant from  $q \sim 600$  MeV/c, especially these MEC related to the virtual excitation of the  $\Delta$  resonance. In our calculations the real excitation of the  $\Delta$  resonance, along with the consequent production of real pions, is not considered. Our nuclear models deal with purely nucleonic degrees of freedom. Experimental transverse responses, such as those shown in Fig. 1, clearly show the presence of the  $\Delta$  resonance peak, with increasing value of the momentum transfer. Our model indicates that MEC do not destroy the scaling in the kinematic range of our interest.

We have also investigated the effects of the SRC, which could also violate the scaling. However, the size of these effects is so small as to be negligible. The main modifications of the mean-field responses are due to the FSI. When we applied the FSI we obtain, even for  $q = 700$  MeV/c, scaling functions very different from those predicted by the RFG model or by the mean-field model and that are rather similar to the empirical one. Moreover, in any case, the FSI do not heavily break the scaling properties. We found that scaling of the first kind is conserved down to  $q = 450$  MeV/c.

We have presented in detail only the results obtained for the electromagnetic transverse and longitudinal responses since, for the weak responses, we found, related to the neutrino scattering processes, analogous results. We can summarize the main points of this first part of our investigation by saying that the effects beyond the RFG model we have considered strongly modify the scaling functions, but they do not destroy their scaling. This explain the good scaling properties of the experimental longitudinal electromagnetic responses, which are not affected by the excitation of the  $\Delta$  resonance, an effect not included in our calculations.

After studying the scaling properties of the various responses we have investigated the reliability of the cross sections predicted by using the scaling functions. The idea is to assume that superscaling is verified (i.e., for all three kinds of scaling we have considered) and then to use the scaling functions to predict the cross sections. The cross sections calculated with our complete model have been compared with those obtained by using as superscaling functions the empirical scaling function fitting the 570-MeV longitudinal data of Ref. [9],  $f_U^{\text{ex}}$ , and our longitudinal scaling function  $f_U^{\text{th}}$ . We have chosen this last scaling function as a theoretical universal scaling function.

We have verified that, in the quasi-elastic peak, the electron scattering cross sections obtained with the full calculation are very close to those obtained with  $f_U^{\text{th}}$ . Also the comparison with the data is rather good. These calculations have been done for momentum transfer values larger than 500 MeV/c; therefore

these results confirm the validity of the superscaling in the quasi-elastic regime. The problems arise in the evaluation of the total neutrino cross sections. In these cross sections, together with the contribution of the quasi-elastic kinematics, where superscaling is satisfied, there is also the contribution of kinematics regions where there is no scaling. We found that the scaling predictions of the total neutrino cross sections are unreliable up to neutrino energies of 200 MeV. At this point the scaling cross sections are 20% larger than those obtained by the full calculation. This difference becomes smaller with increasing neutrino energy, and we found it to be reduced to about 7% at 300 MeV. We stopped our calculations of the total cross section here, since our model is not reliable for larger neutrino energies. The comparison between double differential cross sections calculated at excitation energies of 150 and 200 MeV, for neutrino energies up to 1 GeV, gives an indication that the difference between the total cross sections becomes smaller with increasing neutrino energy. It is worth pointing out, however, that for neutrino energies larger than 300 MeV, the contribution of the  $\Delta$  resonance is no longer negligible, as we have implicitly considered in our calculations.

**ACKNOWLEDGMENTS**

This work has been partially supported by the agreement INFN-CICYT, by the Spanish DGI (FIS2005-03577), and by MURST through the PRIN “Teoria della struttura dei nuclei e della materia nucleare.”

**APPENDIX: THE EXPERIMENTAL SCALING FUNCTIONS**

In this appendix we describe the procedure followed to obtain the experimental scaling functions (SFs) and also the empirical values of the indexes  $\mathcal{D}$  and  $\mathcal{R}$  from the electromagnetic response data of Ref. [9].

The SF data have been obtained by inserting in Eqs. (7) and (8) the values of the experimental responses. The uncertainty on the SF data has been evaluated directly from the same equations, by taking into account the uncertainties of the original response data.

The evaluation of  $\mathcal{D}$  and  $\mathcal{R}$ , Eqs. (32) and (33), requires knowledge of the various SFs at the same  $\Psi$  points. Since the

SF data are given for different values of  $\Psi$ , we fixed a grid of  $\Psi$  values, and we produced pseudo SF data by doing a quadratic interpolation of the SF data previously obtained.

The uncertainties of these pseudo SF data have been obtained by using a Monte Carlo strategy. Associated to each experimental SF point we have generated a new point compatible with the Gaussian distribution related to the experimental uncertainty. These new data formed a set of SF points used to obtain pseudo data on the grid by quadratic interpolation. We repeated this procedure one thousand times, obtaining, for each value of  $\Psi$  of the grid, a distribution of SF points that allowed us to determine the corresponding uncertainty.

After having determined the uncertainties of the pseudo SF data, we calculated the uncertainty of the  $\mathcal{D}$  index as

$$\sigma_{\mathcal{D}} = \sqrt{[f_i^{\max}(\psi_{i_{\max}})]^2 + [f_i^{\min}(\psi_{i_{\max}})]^2},$$

where  $\psi_{i_{\max}}$  is the value where the difference  $f_i^{\max} - f_i^{\min}$  reaches the maximum value.

We have calculated the uncertainty on  $\mathcal{R}$  in two steps. We first evaluated the uncertainty of the sum

$$S = \sum_{i=1, \dots, K} [f_i^{\max} - f_i^{\min}]$$

in the numerator of Eq. (33) by using a procedure analogous to that used to obtain  $\sigma_{\mathcal{D}}$ . That is,

$$\sigma_S = \sqrt{\sum_{i=1, \dots, K} ([f_i^{\max}]^2 + [f_i^{\min}]^2)}.$$

To obtain the global uncertainty, we again used a Monte Carlo strategy, and we calculated the ratio in Eq. (33) one thousand times by sampling the values of  $S$  and of  $f^{\max}$  within the corresponding Gaussian distributions.

The empirical SF, represented by the thin full line in the  $f_L$  panel at 570 MeV/c in Fig. 1, has been obtained as a best fit of all the experimental points shown in the panel. The expression of our fitting function is

$$f_U^{\text{ex}}(\Psi) = \frac{A \exp(-\Psi^2) + B\Psi^2 + C\Psi + D}{(\Psi + E)^2 + F^2}, \quad (\text{A1})$$

with  $A = 0.971$ ,  $B = -0.067$ ,  $C = 0.385$ ,  $D = 0.145$ ,  $E = 0.366$ , and  $F = 1.378$ .

---

[1] W. M. Alberico, A. Molinari, T. W. Donnelly, E. L. Kronenberg, and J. W. Van Orden, *Phys. Rev. C* **38**, 1801 (1988).  
 [2] A. De Pace, *Nucl. Phys.* **A635**, 163 (1998).  
 [3] J. E. Amaro, M. B. Barbaro, J. A. Caballero, T. W. Donnelly, and A. Molinari, *Phys. Rep.* **368**, 317 (2002).  
 [4] C. Maieron, T. W. Donnelly, and I. Sick, *Phys. Rev. C* **65**, 025502 (2002).  
 [5] J. E. Amaro, M. B. Barbaro, J. A. Caballero, T. W. Donnelly, A. Molinari, and I. Sick, *Phys. Rev. C* **71**, 015501 (2005).  
 [6] J. E. Amaro, M. B. Barbaro, J. A. Caballero, T. W. Donnelly, and C. Maieron, *Phys. Rev. C* **71**, 065501 (2005).  
 [7] T. W. Donnelly and I. Sick, *Phys. Rev. Lett.* **82**, 3212 (1999).  
 [8] T. W. Donnelly and I. Sick, *Phys. Rev. C* **60**, 065502 (1999).  
 [9] J. Jourdan, *Nucl. Phys.* **A603**, 117 (1996).  
 [10] M. B. Barbaro, R. Cenni, A. De Pace, T. W. Donnelly, and A. Molinari, *Nucl. Phys.* **A643**, 137 (1998).  
 [11] M. B. Barbaro, J. A. Caballero, T. W. Donnelly, and C. Maieron, *Phys. Rev. C* **69**, 035502 (2004).  
 [12] J. E. Amaro, M. B. Barbaro, J. A. Caballero, and T. W. Donnelly, *Phys. Rev. C* **73**, 035503 (2006).  
 [13] A. N. Antonov, M. V. Ivanov, M. K. Gaidarov, E. Moya de Guerra, P. Sarriguren, and J. M. Udías, *Phys. Rev. C* **73**, 047302 (2006); **74**, 054603 (2006).  
 [14] S. Boffi, C. Giusti, F. Pacati, and M. Radici, *Electromagnetic Response of Atomic Nuclei* (Clarendon Press, Oxford, 1996).  
 [15] A. R. Edmonds, *Angular Momentum in Quantum Mechanics* (Princeton University Press, Princeton, 1968).

- [16] J. M. Blatt and V. F. Weisskopf, *Theoretical Nuclear Physics* (Wiley, New York, 1952).
- [17] G. Hoeler, E. Pietarinen, I. Sabba-Stefanescu, F. Borkowski, G. G. Simon, V. H. Walther, and R. D. Wendling, Nucl. Phys. **B114**, 505 (1976).
- [18] J. E. Amaro, J. A. Caballero, T. W. Donnelly, A. M. Lallena, E. Moya de Guerra, and J. Udias, Nucl. Phys. **A602**, 263 (1996).
- [19] J. S. O'Connell, T. W. Donnelly, and J. D. Walecka, Phys. Rev. C **6**, 719 (1972).
- [20] J. D. Walecka, in *Muon Physics*, Vol. 2, edited by V. W. Hughes and C. S. Wu (Academic Press, New York, 1975), p. 113.
- [21] J. D. Walecka, *Theoretical Nuclear and Subnuclear Physics* (Oxford University Press, New York, 1995).
- [22] J. E. Amaro, G. Co', and A. M. Lallena, Int. J. Mod. Phys. E **3**, 735 (1994).
- [23] A. Botrugno and G. Co', Nucl. Phys. **A761**, 203 (2005).
- [24] F. Arias de Saavedra, G. Co', A. Fabrocini, and S. Fantoni, Nucl. Phys. **A605**, 359 (1996).
- [25] D. Pines, K. Q. Quader, and J. Wambach, Nucl. Phys. **A477**, 365 (1998).
- [26] A. L. Fetter and J. D. Walecka, *Quantum Theory of Many-Particle Systems* (McGraw-Hill, San Francisco, 1971).
- [27] A. M. Lallena, Nucl. Phys. **A615**, 325 (1996).
- [28] M. Anguiano, G. Co', A. M. Lallena, and S. R. Mokhtar, Ann. Phys. (NY) **296**, 235 (2002).
- [29] M. Anguiano, G. Co', and A. M. Lallena, J. Phys. G **29**, 1119 (2003).
- [30] M. Anguiano, G. Co', and A. M. Lallena, Nucl. Phys. **A744**, 168 (2004).
- [31] J. E. Amaro, G. Co', and A. M. Lallena, Nucl. Phys. **A578**, 365 (1994).
- [32] G. Co' and A. M. Lallena, Ann. Phys. (NY) **287**, 101 (2001).
- [33] F. Arias de Saavedra, G. Co', and M. M. Renis, Phys. Rev. C **55**, 673 (1997).
- [34] J. E. Amaro, G. Co', and A. M. Lallena, in *Quasielastic Electron Scattering in Nuclei*, edited by R. Cenni (Nova Science, New York, 2001), p.63.
- [35] G. Co', K. F. Quader, R. D. Smith, and J. Wambach, Nucl. Phys. **A485**, 61 (1988).
- [36] R. D. Smith and J. Wambach, Phys. Rev. C **38**, 100 (1998).
- [37] C. Bleve, G. Co', I. De Mitri, P. Bernardini, G. Mancarella, D. Martello, and A. Surdo, Astropart. Phys. **16**, 145 (2001).
- [38] G. Co', C. Bleve, I. De Mitri, and D. Martello, Nucl. Phys. B, Proc. Suppl. **112**, 210 (2002).
- [39] R. M. Sealock *et al.*, Phys. Rev. Lett. **62**, 1350 (1989).
- [40] M. Anghinolfi *et al.*, Nucl. Phys. **A602**, 405 (1996).
- [41] C. Williamson *et al.*, Phys. Rev. C **56**, 3152 (1997).